Evolution of the electronic excitation spectrum with strongly diminishing hole density in superconducting $Bi_2Sr_2CaCu_2O_{8+\delta}$

J. W. ALLDREDGE[1], JINHO LEE[1,2], K. McELROY[3], M. WANG[1], K. FUJITA[1], Y. KOHSAKA[1,4], C. TAYLOR[1], H. EISAKI[5], S. UCHIDA[6], P. J. HIRSCHFELD[7] AND J. C. DAVIS[1,8]*

[1]LASSP, Department of Physics, Cornell University, Ithaca, New York 14850, USA
[2]School of Physics and Astronomy, University of St Andrews, North Haugh, St Andrews KY16 9SS, Scotland
[3]Department of Physics, University of Colorado, Boulder, Colorado 8030, USA
[4]Magnetic Materials Laboratory, RIKEN, Wako 351-0198, Japan
[5]NI-AIST, 1-1-1 Central 2, Umezono, Tsukuba, Ibaraki 305-8568, Japan
[6]Department of Physics, University of Tokyo, Tokyo 113-8656, Japan
[7]Department of Physics, University of Florida, Gainesville, Florida 32611, USA
[8]CMP&MS Department, Brookhaven National Laboratory, Upton, New York 11973, USA
*e-mail: jcdavis@ccmr.cornell.edu

Published online: 23 March 2008; doi:10.1038/nphys917

Coulomb interactions between the carriers may provide the mechanism for enhanced unconventional superconductivity in the copper oxides. However, they simultaneously cause inelastic quasiparticle scattering that can destroy it. Understanding the evolution of this balance with doping is crucial because it is responsible for the rapidly diminishing critical temperature as the hole density p is reduced towards the Mott insulating state. Here, we use tunnelling spectroscopy to measure the $T \rightarrow 0$ spectrum of electronic excitations $N(E)$ over a wide range of hole density p in superconducting $Bi_2Sr_2CaCu_2O_{8+\delta}$. We introduce a parameterization for $N(E)$ based on a particle–hole symmetric anisotropic energy gap $\Delta(\mathbf{k}) = \Delta_1(\cos(k_x) - \cos(k_y))/2$ plus an inelastic scattering rate that varies linearly with energy $\Gamma_2(E) = \alpha E$. We demonstrate that this form of $N(E)$ enables successful fitting of differential tunnelling conductance spectra throughout much of the $Bi_2Sr_2CaCu_2O_{8+\delta}$ phase diagram. We find that Δ_1 values rise with falling p along the familiar trajectory of excitations to the 'pseudogap' energy, whereas the energy-dependent inelastic scattering rate $\Gamma_2(E) = \alpha E$ seems to be an intrinsic property of the electronic structure and rises steeply for $p < 16\%$. Such diverging inelastic scattering may play a key role in suppression of superconductivity in the copper oxides as the Mott insulating state is approached.

Hole-doped copper oxides have their highest superconducting critical temperature T_c at hole densities per CuO_2 of $p \sim 16\%$, and the superconductive state exhibits d-wave symmetry. By measuring scanning tunnelling microscopy (STM) tip–sample differential conductance $dI/dV(\mathbf{r}, V) \equiv g(\mathbf{r}, V)$ at each location $\mathbf{r}$ and bias voltage V one can achieve energy-resolved images of the local density of excitations $N(E)$ because $g(\mathbf{r}, V) \propto N(\mathbf{r}, E = eV)$ (when the $N(E)$ integrated to the junction formation bias is homogeneous[1]). Near optimal doping, the $g(V)$ spectra seem highly consistent with the theoretical $N(E)$ of a d-wave superconductor; when superconductivity is suppressed by unitary scattering at a Zn atom[2,3] or at the centre of a vortex core[3,4], the two particle–hole symmetric peaks in $g(V)$ are also suppressed as expected of the superconducting coherence peaks. Thus, there can be little doubt that the measured $N(E)$ near optimal doping is that of the d-wave superconducting state. But as p is reduced, the electronic excitations begin to exhibit[5–7] a 'pseudogap'. This is a momentum-space anisotropic energy gap[5–9] in the excitation spectrum, the effect of which can be detected by numerous spectroscopic and thermodynamic techniques[6,7] far above the superconducting T_c (which diminishes to zero as $p \rightarrow 0$). The pseudogap energy scale increases linearly with diminishing p.

Possible explanations for the pseudogap include, for example, effects of hole doping an antiferromagnetic Mott insulator[10–14]. Different models for this situation yield an anisotropic energy gap, the maximum of which diminishes linearly with increasing p (heuristically, this can be viewed as a dilution of the antiferromagnetic exchange energy by the holes). But an alternative type of proposal has been that the pseudogap is due to some distinct electronic phase[15–18], the anisotropic energy gap of which represents the breaking of a different symmetry. Measurements solely of the pseudogap energy scale versus p have not resulted in discrimination between these two types of proposal and no consensus exists for the cause of the pseudogap in the electronic excitations of copper oxides[5–7].

A fully detailed knowledge of the $T \rightarrow 0$ intrinsic spectrum of electronic excitations as a function of doping could help break this impasse. The lifetimes of 'nodal' excitations—those with $\mathbf{k} \parallel (\pi, \pi)$—have been widely studied[19–22]; these states are not the focus of study here. Instead, we focus primarily on

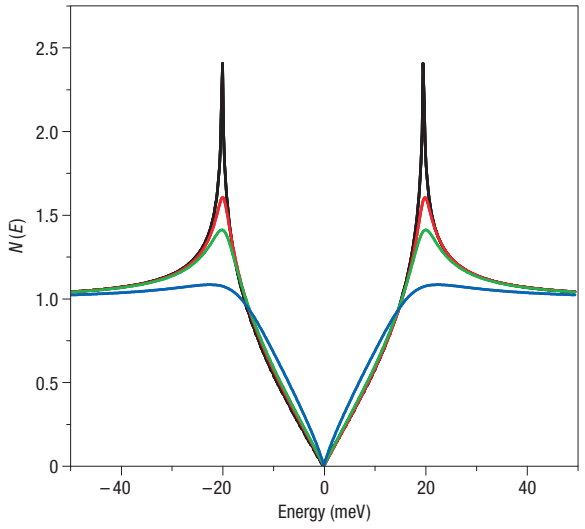

Figure 1 Theoretical effect of $\Gamma_2 = \alpha E$ inelastic scattering on the density of states $N(E)$. Representative $N(E)$ from equation (2) demonstrating the effect of increasing α for $\Delta_1 = 20$ meV. The black line represents $\alpha = 0$, the red line $\alpha = 0.05$, the green line $\alpha = 0.10$ and the blue line $\alpha = 0.40$.

higher-energy excited states that reach all the way to the antinodes $\mathbf{k} \sim (\pi, 0):(0, \pi)$. Scattering rates for these states have been studied in the superconducting[23] and non-superconducting[24] state at or above optimal doping, revealing strong momentum-space anisotropy of the scattering rate at the Fermi surface. And, using optical techniques, Gedik *et al.* stimulated these non-nodal excited states and discovered that a marked change in their recombination rate occurs near optimal doping[25]. Despite these recent advances, knowledge of the $T \to 0$ spectrum of electronic excitations sufficient to constrain the models, does not yet exist.

Here, we introduce a new technique for understanding the spatial and doping dependence of the electronic excitation spectrum $N(E)$ of superconducting cuprates. We use single crystals of $Bi_2Sr_2CaCu_2O_{8+\delta}$ (Bi-2212) grown by the floating-zone method. Atomically clean and flat surfaces of BiO are achieved and maintained by cleaving the samples in cryogenic ultrahigh vacuum before insertion into the STM at $T = 4.2$ K. We report on samples with six different hole densities $0.08 \leq p \leq 0.22$ (± 0.01), each within a 40 nm square field of view and, in total, comprising more than 10^6 individual $g(\mathbf{r}, V)$ spectra. Our objective is to use this comprehensive data set to explore the evolution with doping of the electronic excitation spectra.

In *s*-wave superconductors, an increasing quasiparticle inelastic scattering rate reduces their lifetimes and eventually destroys the superconductivity[26]. The signature of this process is manifest in $g(V)$; at zero temperature and with no scattering, two 'coherence' peaks in $g(V)$ occur as singularities on either side of an empty gap and, as scattering rates increase, these peaks decrease in height and increase in width with a rapid increase of the density of excitations near $E = 0$. Such $g(V)$ spectra can be very successfully parameterized by adding an imaginary term Γ_1 to the quasiparticle energy E so that $N(E)$ takes the form[27]

$$N(E, \Gamma) = A \times \mathrm{Re}\left(\frac{E + i\Gamma_1}{\sqrt{(E + i\Gamma_1)^2 - \Delta^2}}\right). \qquad (1)$$

Here, Γ_1 represents a constant scattering rate for quasiparticles. As Γ_1 is increased keeping Δ constant, the coherence peaks diminish, the peak–peak measure of the energy-gap becomes less well defined and there is a rapid increase of $N(0)$—all in excellent agreement with the experimentally observed effects in $g(V)$.

Our goal is to extend this approach to the cuprate excitation spectra. The $N(E)$ we propose is (at least formally) a natural extension of equation (1)

$$N(E, \Gamma_2) = A \times \mathrm{Re}\left(\left\langle \frac{E + i\Gamma_2(E)}{\sqrt{(E + i\Gamma_2(E))^2 - \Delta(k)^2}} \right\rangle_{fs}\right) + B \times E. \qquad (2)$$

Here, $\Delta(\mathbf{k}) = \Delta_1(\cos(k_x) - \cos(k_y))/2$ is a particle–hole symmetric anisotropic energy gap. We could also introduce a term $i\Gamma_1$ representing a constant scattering rate from near-unitary scatterers (analogous to equation (1)), but we find it plays a subsidiary role herein. In contrast, the $\Gamma_2(E) = \alpha E$ term, which represents an effective scattering rate that is linear in energy, plays a key role. In equation (2), A is a normalization factor and B is a linear asymmetry term to deal with the ubiquitous background slope of $g(V)$ of Bi-2212. Equation (2) then represents the $N(E)$ function that we fit to each measured $g(V)$ (its exact form is determined over the appropriate Fermi surface at each doping[28]—see the Supplementary Information). Figure 1 shows examples of the $N(E)$ calculated from equation (2) as α increases (Δ_1 remaining constant). We see that the peaks are rapidly suppressed but, because $\Gamma_2(0) = 0$, an approximately V-shaped gap centred on the chemical potential is retained for all scattering rates. This is crucial for the successful parameterization of all $g(E)$ because, throughout the majority of the Bi-2212 phase diagram, such characteristics are ubiquitous.

We use data sets consisting of atomically resolved and registered $g(\mathbf{r}, V)$ maps spanning the range of doping $0.08 \leq p \leq 0.22$ (as determined from $T_c = 95\,\mathrm{K} \times (1 - 82.6\,(p - 0.16)^2)$ along with other techniques). Their spectra change continuously from quite small gaps ($\Delta_1 \sim 10$ meV) with sharp particle–hole symmetric peaks, to large ($\Delta_1 \sim 65$ meV) gaps where the vestigial peaks can just be resolved[29], to the V-shaped gaps with no apparent peaks that predominate below $p \sim 10\%$ (refs 1,30). To complicate matters further, at each doping there is a distribution in excitation spectra associated with the distribution of non-stoichiometric oxygen dopant atoms[31], with the probability of these different spectral types varying with doping[4,29–31]. Fitting equation (2) to all of these spectra is designed to yield quantitative values for both $\Gamma_2(E)$ and Δ_1—even when there are no peaks visible and despite both the electronic disorder and the rapid changes in spectral types with doping.

Figure 2 shows the distribution of spectral types[29,30] from within a single field of view, each curve being offset vertically for clarity. The open circles represent the average $g(V)$ spectrum associated with each energy-gap magnitude—the error bars showing the 1σ variations of each distribution (see the Supplementary Information). This averaging process is designed to yield the characteristic excitation spectrum associated with each energy-gap maximum while minimizing complications from the spatial variations in $g(\mathbf{r}, V)$. We emphasize, however, that our fits of $N(E)$ are to each individual local $g(\mathbf{r}, V)$ spectrum (see the Supplementary Information). The solid lines in Fig. 2 show the average of the fits of equation (2) to the $g(V)$ data—again with all $N(E)$ exhibiting the same Δ_1 averaged together. It is striking how well a very wide variety of $g(V)$ spectral shapes, ranging from those exhibiting sharp particle–hole symmetric peaks to those with V-like spectra having no apparent peaks, can be fitted using equation (2). The fit-quality parameter is a normalized $\chi^2 < 0.01$ for more than 90% of the spectra $0.1 \leq p \leq 0.22$. For the sixth sample with

$p \sim 0.08$, the normalized χ^2 remains higher because the strong tunnelling asymmetry[1] prevents good fits. And for $p > 0.22$, the spectral shape begins to change in a fashion not yet understood. Nevertheless, the vast majority of measured $g(\mathbf{r}, V)$ spectra for $8\% < p < 22\%$ can be fitted very well (a normalized $\chi^2 < 0.01$) using equation (2). We show in the Supplementary Information typical examples of the fit for each value of Δ_1.

In previous studies of nanoscale electronic disorder in Bi-2212, a local energy-gap maximum Δ_{pp} was defined as half the energy difference between two particle–hole symmetric peaks in $g(V)$ (wherever such pairs of peaks existed). Figure 3, column 1 shows the spatial and doping dependence of such Δ_{pp} maps (all fields of view are 40 nm square and all gap scales are the same with white indicating an inability to measure Δ_{pp} because the peaks could not be identified in high gap regions[29,30]). Figure 3, column 2 shows the spatial and doping dependence of Δ_1 maps calculated from fits of equation (2) to the identical data sets. We see immediately that the Δ_1 maps closely resemble the Δ_{pp} maps. Furthermore, the normalized cross-correlation[31] between all simultaneous pairs of Δ_1 maps and Δ_{pp} maps shown exceeds 0.9 (where identical images would yield 1). These correspondences between Fig. 3, columns 1 and 2 give strong confidence that the equation (2) fitting scheme is working well because the mathematical procedures to make the two kinds of map are completely different.

New information is immediately available from measurements of the gap maximum Δ_1. A limitation of previous studies was that, when there were weak or no peaks in $g(V)$ at low doping, it became virtually impossible to determine Δ_{pp} (such areas were represented in black in refs 29–31 and white in Fig. 3, column 1). But Fig. 2 shows clearly that with strong effective scattering rates $\Gamma_2(E)$, the particle–hole symmetric peaks should disappear and the density of excited states should appear as a V-shaped spectrum. Therefore, Δ_1 can now be extracted in regions where previously it would have been considered unknown. For example, in Fig. 3, column 2 the black regions now represent measured values Δ_1 rising to above 100 meV in small nanoscale patches at our lowest dopings. The extracted values of Δ_1 (Figs 3,4) follow the doping dependence of the pseudogap energy scale[5–7]. Moreover, we find no distinction in terms of the fitted form of $N(E)$ between excitations to the pseudogap energy scale at low dopings, and the familiar excitations of the superconducting state[2–4] at higher dopings and lower energies.

On the basis of accurate mapping of Δ_1 (for example, Fig. 3, column 2), we can also examine the doping dependence of electronic disorder for the pseudogap energy scales. Figure 4a–f shows these Δ_1 maps, but now each is normalized to the mean value of Δ_1 from that same map and shown using the same colour scale. Remarkably, we cannot distinguish which doping is represented by the images in Fig. 4a–f. Figure 4g shows the histograms of $\Delta_1/\bar{\Delta}_1$ from these images; it is immediately obvious that the distributions are virtually independent of doping. This indicates that the nanoscale trigger for energy-gap disorder is universal (as it should be for disorder from interstitial substitutions and dopant atoms[31]). Furthermore, because the same fractional distribution about the mean gap energy is observed for pseudogap energy scales at the low dopings (as $T_c \to 0$), the high-energy pseudogap excitations[32] seem equally susceptible to nanoscale electronic disorder as those of the superconductor[4,29–31].

Next, we focus on the most significant discrepancies between fits to equation (2) and the related $g(\mathbf{r}, V)$ data. These occur predominantly at the 'kinks' that have been reported ubiquitously[1,29–33] in cuprate STM spectra. In general, these kinks are weak perturbations to $N(E)$ near optimal doping, becoming more clear within nanoscale regions; the number of detected kinks increases as p is strongly diminished[29,30]. Figure 5a shows

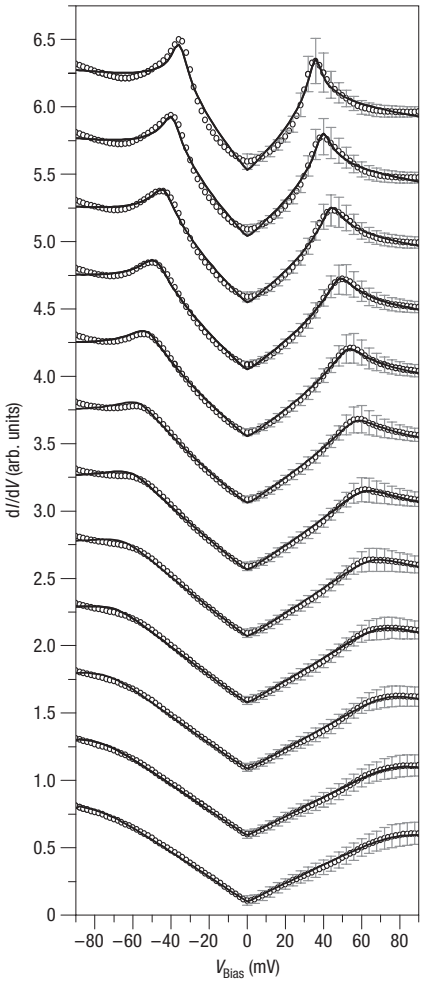

Δ_1 (meV)	Γ_2^* (meV)
38	1.2
43	2.2
48	3.7
53	5.2
57	7.3
62	10.4
67	13.7
72	17.1
77	19.5
82	21.7
87	25.4
92	30.0

Figure 2 Fits of equation (2) $N(E)$ to the average $g(V)$ spectrum for each gap magnitude. Open circles represent the average value of $g(V)$ from all spectra (in one sample with $p = 10\%$) that exhibit a given gap magnitude Δ_1. The error bars give one standard deviation of the distribution in $g(V)$ at each V. The corresponding average of the fits of all spectra by equation (2) are shown as solid lines. The table shows the fitted values of Δ_1 and $\Gamma_2^* = \Gamma_2\,(E = \Delta_1)$. Δ_1 ranges from 38 mV to 93 mV, whereas Γ_2^* spans from below 1 meV to above 25 meV. Each spectrum is offset for clarity. Notice the particle–hole symmetry throughout.

representative Δ_1-sorted spectra. Note that it is for $\Delta_1 > 50$ meV (with equivalent data for all dopings shown in the Supplementary Information) that the kinks become more obvious. Each kink is identified by finding the point of inflection as the minimum in the next derivative $\mathrm{d}^2I/\mathrm{d}V^2$, as shown in Fig. 5b; its energy is labelled $\Delta_0(\mathbf{r})$. We emphasize that these kinks are weak departures from the fits to $N(E)$ (see Supplementary Information, Fig. S4). For the higher energies approaching Δ_1 that are the focus of our study, the kinks neither spoil the fit quality nor the extracted $\Gamma_2(E)$ (see Supplementary Information, Fig. S2). Simultaneous $\Delta_1(\mathbf{r})$ and kink-energy $\Delta_0(\mathbf{r})$ maps can then be derived and are shown in Fig. 5c,d. By imaging $\Delta_0(\mathbf{r})$ for all dopings, we find that the excitations are always divided into two categories: $E < \Delta_0$ excitations are homogeneous in $\mathbf{r}$ space and well-defined d-wave quasiparticle eigenstates in $\mathbf{k}$ space[34,35], whereas for $E > \Delta_0$ they are heterogeneous[29–33] and ill-defined in $\mathbf{k}$ space. Thus, $\langle\Delta_0(\mathbf{r})\rangle$ represents the average energy scale separating spatially homogeneous from heterogeneous excitations.

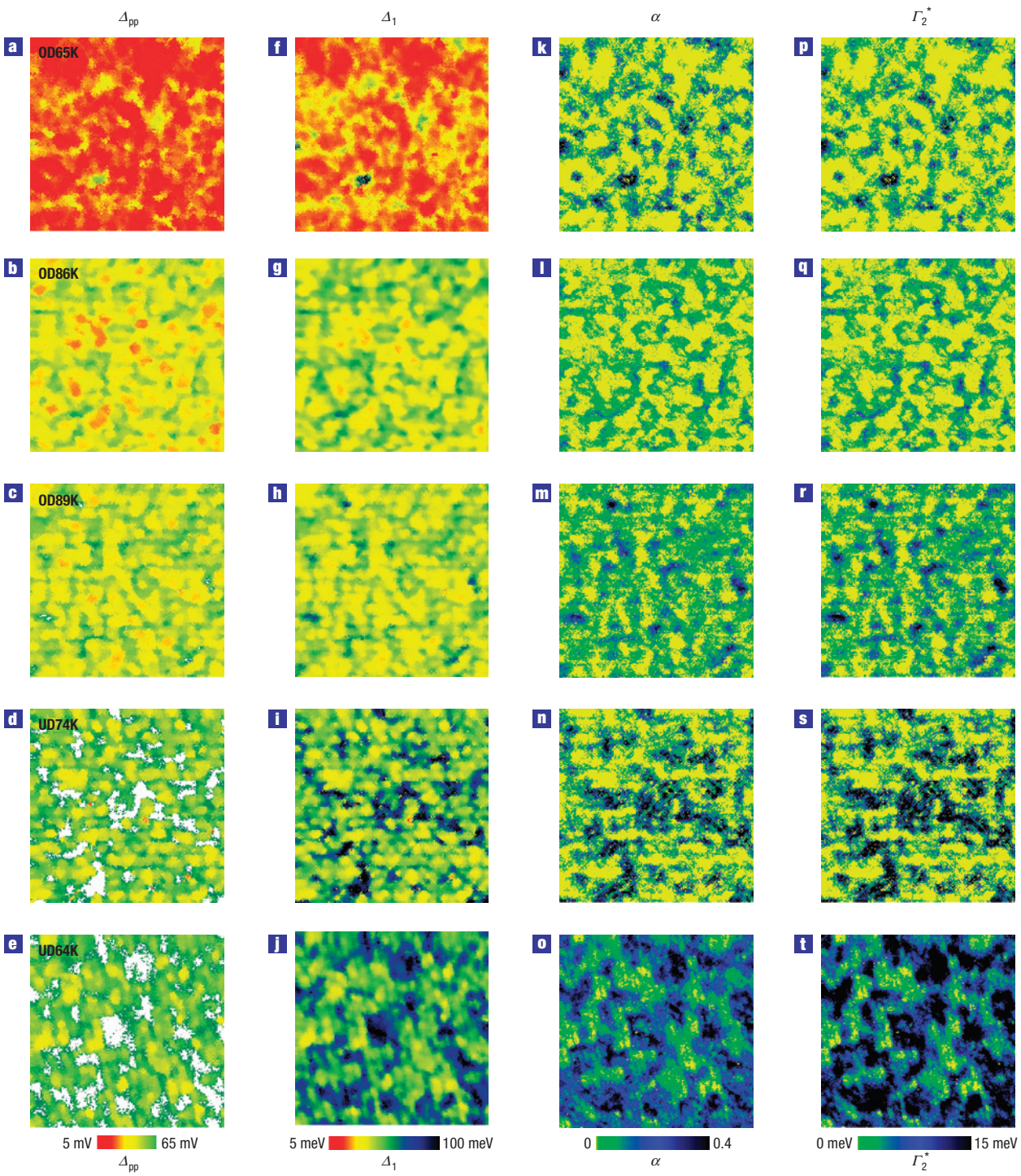

Figure 3 Correlations between spatial arrangements of Δ_{pp}, Δ_1, α and Γ_2^* versus hole density *p*. a–e, Δ_{pp} maps as a function of doping—each for a 40 nm^2 field of view, the white areas are places where Δ_{pp} cannot be defined. The dopings are calculated from the T_c values of the samples using the formula $T_c = 95\,\mathrm{K} \times (1 - 82.6\,(p - 0.16)^2)$ and corroborated by other techniques: 0.22 ± 0.01 (**a**), 0.19 ± 0.01 (**b**), 0.17 ± 0.01 (**c**), 0.14 ± 0.01 (**d**) and 0.10 ± 0.01 (**e**). Tunnelling asymmetry renders fitting the sixth data set at $p \sim 8\%$ impossible. **f–j**, Δ_1 maps calculated from the fits to equation (2) using the identical original $g(\mathbf{r}, V)$ maps as in column 1. Note that where Δ_{pp} and Δ_1 can both be evaluated they create virtually identical patterns. **k–o**, $\alpha(\mathbf{r})$ calculated concurrently with each Δ_1 from the fits to equation (2). **p–t**, The corresponding maximum effective scattering-rate maps Γ_2^*, calculated from columns 2 and 3. Note that Δ_1, α and Γ_2^* create very similar patterns. T_c for each sample is shown in the left panels.

Another breakthrough involves the capability to estimate local effective scattering rates. Images of the coefficient $\alpha(\mathbf{r})$, the linear coefficient of the energy dependence of Γ_2, are shown in Fig. 3, column 3. These $\alpha(\mathbf{r})$ range from 0 to 0.4 (yellow to black) with the spatially averaged value $\langle\alpha(\mathbf{r})\rangle$ growing with falling doping. The scattering rates Γ_2^* at $E = \Delta_1$ are most physically significant.

These are determined from $\Gamma_2^*(\mathbf{r}) = \alpha(\mathbf{r})\Delta_1(\mathbf{r})$ and are shown in Fig. 3, column 4; they range from yellow (weak scattering) to black (strong scattering) with the maximum effective scattering rates $\Gamma_2^* > 25$ meV for $p \leq 10\%$. The direct correspondence between both the coefficients $\alpha(\mathbf{r})$ and $\Gamma_2^*(\mathbf{r})$ with $\Delta_1(\mathbf{r})$ can be seen by comparing columns 2, 3 and 4. From these, it seems that the relationship between $\Delta_1(\mathbf{r})$, $\alpha(\mathbf{r})$ and $\Gamma_2^*(\mathbf{r})$ is intrinsic and local at the nanoscale.

Figure 6a shows the value of α associated with each value of Δ_1 throughout six samples with different hole densities. Overlaid on these data as solid black circles are the $\langle\alpha(\mathbf{r})\rangle$ versus the spatially averaged $\langle\Delta_1\rangle$ for each sample; they are in good agreement with the relationship between local pairs of Δ_1 and α values throughout. These data demonstrate that the relationship between $\Delta_1(\mathbf{r})$:$\alpha(\mathbf{r})$ pairs is local at the nanoscale and apparently intrinsic—because it is the same in all samples at all dopings. Again, we conclude that whatever electronic process perturbs the energy-gap distribution[29–33,36] perturbs the effective scattering rate $\Gamma_2(E)$ locally in a related fashion.

Significant new insights emerge from these fits when summarized in the form of a phase diagram. Figure 6b shows $\langle\Delta_1\rangle$ as blue circles; it rises linearly with decreasing p along the well-known[5–7] trajectory for excitations to the pseudogap energy scale. The black circles represent the spatially averaged $E = \Delta_1$ scattering rates $\langle\Gamma_2^*\rangle$; these are very low when $p > 16\%$ but undergo a strong transition to a steeply rising trajectory for $p < 16\%$. This marked increase of the effective scattering rates for states away from the nodes culminates in another transition somewhere below $p \sim 10\%$ with the appearance of extreme tunnelling asymmetry[1,30] (rendering efforts to fit equation (2) impossible). Finally, the red circles represent the spatial average of the second energy scale $\langle\Delta_0\rangle$ where both the ubiquitous 'kink' in the $g(\mathbf{r}, V)$ spectrum occurs, and above which spatial homogeneity in quasiparticle excitations is lost. Clearly $\langle\Delta_0\rangle$ diverges from $\langle\Delta_1\rangle$, falling slowly as $p \to 0$.

DISCUSSION

Here, we introduce a new technique for analysing the tunnelling-derived cuprate electronic excitation spectrum $N(E)$ as $T \to 0$. The results provide a significantly more quantitative and comprehensive picture of the $T \to 0$ excitations than was previously available and for a wide range of hole densities. And, because this fitting technique is demonstrably successful under a very wide variety of circumstances, we can also anticipate its extension to new arenas such as at high temperatures[32] or when further phase fluctuation effects occur near vortex cores[4]. It is important, however, to be aware of the limitations of any interpretation of $\Gamma_2(E)$ simply as a one-particle scattering rate. Equation (2) might be taken as an expression for a classic d-wave superconductor with single-particle scattering rate Γ_2 within Bardeen–Cooper–Schrieffer theory. Such an interpretation, which may possibly be appropriate in the overdoped materials, would assume weakly interacting quasiparticles. But as the Mott insulator is approached at strong underdoping, this intrinsic effective scattering rate may become so intense that such single-particle $\mathbf{k}$-space excitations are no longer well defined even in the superconducting state (especially near the Brillouin zone face)[8,9,21,23,25]. Only a few authors have investigated theoretically the lifetime of such quasiparticles in the superconducting state and away from the nodes. Spin fluctuation theories of d-wave superconductivity suggest relatively weak dependence of the scattering rate on the direction of the quasiparticle momentum[37,38]. In the underdoped cuprates, pair-breaking scattering from vortex–antivortex pairs has been proposed as the origin of large angle-resolved photoemission spectroscopy spectral widths near the antinode[39,40]. Another caution about the

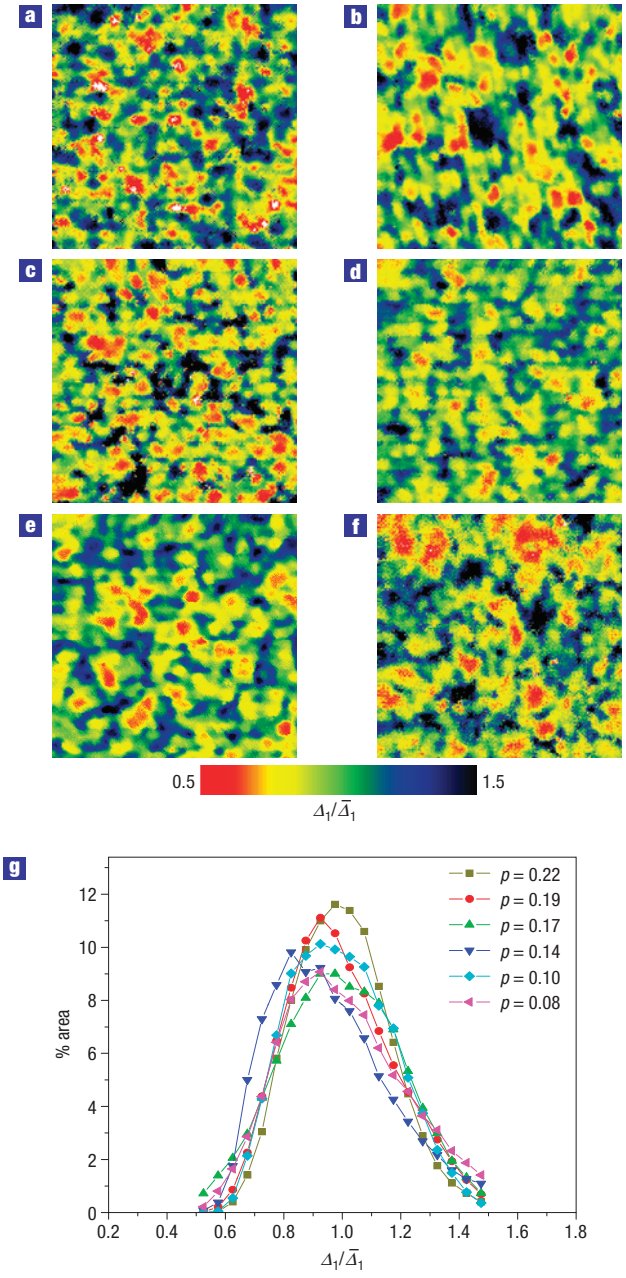

Figure 4 Doping dependence of spatial arrangements of $\Delta_1(r)$ normalized by mean value of Δ_1. a–f, Normalized Δ_1 maps for six hole densities $0.8 < p < 0.22$ for 40 nm^2 $g(\mathbf{r}, V)$ data sets. The dopings are 0.08 (**a**), 0.10 (**b**), 0.14 (**c**), 0.17 (**d**), 0.19 (**e**) and 0.22 (**f**). The maps were normalized to the average value of Δ_1 in each $g(\mathbf{r}, V)$ map. For $p = 0.08$, we can only estimate the value of Δ_1 from fits to the positive bias part of the spectrum where the steep tunnelling asymmetry is less prominent. **g**, Histograms of the data in **a–f**. Obviously, these distributions are statistically highly similar.

effective scattering rate Γ_2 discussed here is that it is related to the local Green's function $G(\mathbf{r}, \mathbf{r})$, the spectral characteristics of which will be broadened by scattering processes involving the entire Fermi surface. It is then far from clear that a general fit of the form of equation (2) with a local self-energy should succeed; in an inhomogeneous system, the self-energy is a bilocal quantity $\Sigma(\mathbf{r}, \mathbf{r}')$. Our findings that the vast majority of spectra can be fitted, at least for $E > \Delta_0$, by an identical form as

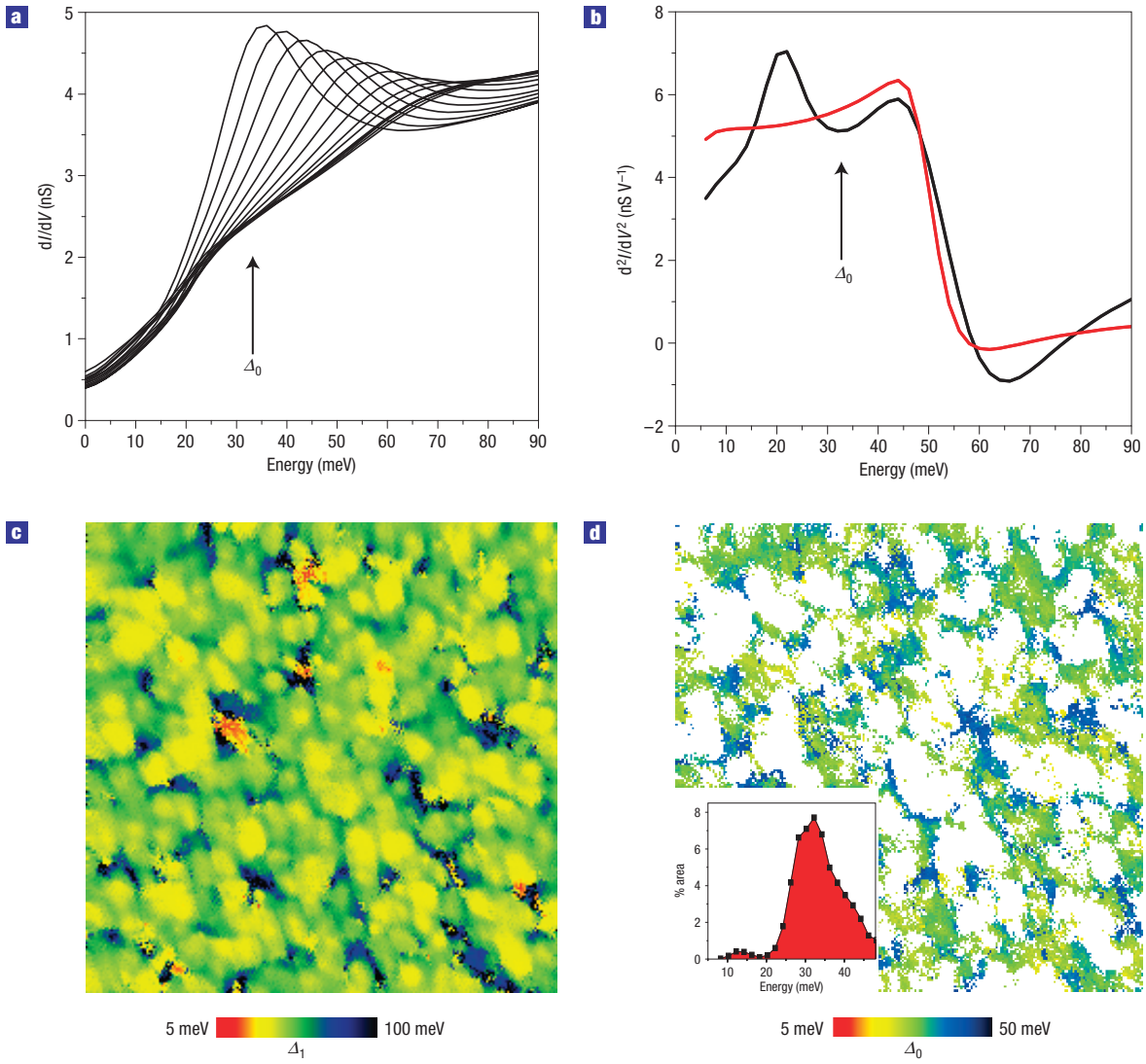

Figure 5 Spatial arrangements of kink energy $\Delta_0(\mathbf{r})$ that separates homogeneous from heterogeneous electronic structure. a, A set of Δ_1-sorted spectra shown with an expanded vertical scale designed to emphasize the representative kinks occurring ubiquitously in $\Delta_1 > 50$ meV spectra. The arrow labelled Δ_0 points to the average energy at which such kinks are detected in dI/dV. **b**, The energy of each kink $\Delta_0(\mathbf{r})$ is identified by finding the point of inflection as the minimum in the next derivative d^2I/dV^2. The black line is the spatially averaged value of d^2I/dV^2; the red line is the spatially averaged derivative of the fits to equation (2) and the arrow labelled Δ_0 indicates the kink energy. **c**, Gap-energy $\Delta_1(\mathbf{r})$ map. **d**, Kink-energy map $\Delta_0(\mathbf{r})$ simultaneous with **c**. Clearly the kinks are associated with the higher-energy gap spectra, and this observation is found to be true at all dopings described herein. The inset shows the distribution of the detected kink energies in the field of view.

equation (2) and that $\Gamma_2(\mathbf{r})$ is spatially correlated with $\Delta_1(\mathbf{r})$, imply that $\Gamma_2(\mathbf{r})$ does represent the effective 'local' self-energy of a quasiparticle sampling a region of size less than or equal to the gap 'patch' size, that is, the system is self-averaging on this scale. A final caveat is that $\Gamma_2(E) = \alpha E$ represents the first approximation to the true energy dependence of scattering rates consistent with the spectra; it captures very well the low scattering of near-nodal quasiparticles and the intense scattering Γ_2^* at $E = \Delta_1$. Eventually, however, a more complex form for $\Gamma_2(E)$ consistent with everything reported herein but capturing finer details of changes in scattering rate throughout $\mathbf{k}$ space may be required.

Nevertheless, a number of important conclusions result from these data and fitting procedures. Local quasiparticle lifetimes $\tau(E) \sim 1/\Gamma_2(E)$ can now be determined from STM data. If we focus on $\langle\Gamma_2\rangle$ as a function of p, we find a very distinct change near optimal doping characterized by the appearance and extremely rapid growth of inelastic scattering rates towards the underdoped regime. This latter effect signifies such intense scattering near the antinodes at lowest dopings, that it must be closely related to the disappearance[8,9] of well-defined $\mathbf{k}$ states there. Moreover, $\Delta_1(\mathbf{r})$ and the coefficient of energy dependence in the effective scattering rate $\alpha(\mathbf{r})$ seem to be linked intrinsically and locally—retaining the same relationship throughout all samples. The rapid increase of Γ_2^* scattering rates as the Mott insulator state is approached is probably due to electron–electron interactions, but the exact microscopic processes cannot be identified from this study. Significantly, we find no apparent distinction in terms of the form of $N(E)$ in equation (2) between fits to optimally doped $g(V)$ spectra that definitely represent d-wave superconductivity,

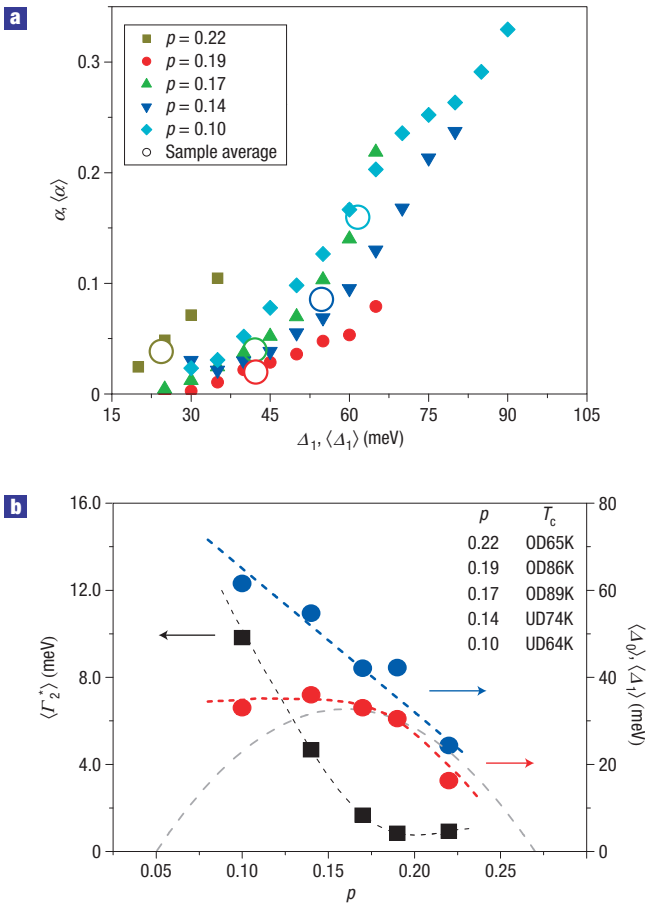

Figure 6 Local and global relationships between α and Δ_1 plus 'phase diagram' of $\langle\Delta_1\rangle$, $\langle\Delta_0\rangle$ and $\langle\Gamma_2^*\rangle$. a, The local relationship between $\alpha(\mathbf{r})$ and $\Delta_1(\mathbf{r})$ using all of the $N(E)$ fits for the average hole densities $\langle p\rangle$ shown. The spatial average value of $\langle\Delta_1\rangle$ and $\langle\alpha\rangle$ for each of the five different samples is plotted as large coloured circles. The global average relationship between $\langle\Delta_1\rangle$ and $\langle\alpha\rangle$ seems to be indistinguishable from the local relationship between $\alpha(\mathbf{r})$ and $\Delta_1(\mathbf{r})$. **b**, The doping dependence of fitted $\langle\Delta_1\rangle$ (blue circles), $\langle\Delta_0\rangle$ (red circles) and $\langle\Gamma_2^*\rangle$ (black squares), each set interconnected by dashed guides to the eye. The higher-scale $\langle\Delta_1\rangle$ evolves along the pseudogap line[5–7], whereas the lower-scale $\langle\Delta_0\rangle$ represents segregation in energy between homogeneous and heterogeneous electronic structure. The separation of $\langle\Delta_1\rangle$ from $\langle\Delta_0\rangle$ scales begins to occur at the point where $\langle\Gamma_2^*\rangle$ starts to rise rapidly. T_c and p for each sample are shown.

and the $g(V)$ spectra of strongly underdoped samples down to $p \sim 10\%$ as the superconducting T_c diminishes towards zero. This means that a combination of an anisotropic and particle–hole symmetric gap to excitations $\Delta(\mathbf{k}) = \Delta_1(\cos(k_x) - \cos(k_y))/2$ plus an effective scattering rate $\Gamma_2(E) = \alpha E$ provides a good description of excitation spectra—without recourse to another coexisting electronic ordered state. We emphasize that these conclusions might not hold at $p < 10\%$ because spectra are no longer well fitted by equation (2) owing to strong tunnelling asymmetry[1]. Furthermore, our results for $p > 10\%$ do not imply that there is only one energy scale present: consistent with both the wide variety of long-standing results[6,7,9,25,29,30,33] and the more recent spectroscopic observations[41–43], we find that two energy scales always exist on the underdoped side of the phase diagram. The higher-scale $\langle\Delta_1\rangle$ evolves along the pseudogap line. Here, we find that the lower-scale $\langle\Delta_0\rangle$ (representing segregation in energy between homogeneous and manifestly d-wave superconductive[34] low-energy electronic structure and the heterogeneous high-energy electronic structure) diverges from $\langle\Delta_1\rangle$ when the Γ_2 scattering rates begin to increase rapidly.

An intriguing scenario stimulated by these observations would be that superconducting cuprates exhibit an anisotropic/particle–hole symmetric excitation energy scale $\Delta(\mathbf{k}) = \Delta_1(\cos(k_x) - \cos(k_y))/2$ but that the electronic excitations experience rapidly increasing inelastic scattering rates as $p \to 0$. This scenario has recently become the focus of intense theoretical study[44] yielding a number of far-reaching conclusions including (1) realistic calculations of impurity- and spin-fluctuation scattering contributions to local density of states showing that typical quasiparticle scattering rates are indeed quasilinear in energy and proportional to Δ_1, (2) demonstration of how the mean free path falls markedly with increasing quasiparticle energy so that, below a critical bias, all quasiparticles explore so many heterogeneous gap patches that their spectra seem homogeneous, (3) evidence that the quasiparticle interference modulations[34,35] could be weakened primarily by inelastic scattering represented by $\Gamma_2(E)$ and (4) reconciliation of photoemission with STM tunnelling and neutron-scattering lifetimes, by inclusion of gap-inhomogeneity-induced broadening of the angle-resolved photoemission spectroscopy spectral function. Moreover, quasiparticles subject to scattering rates above some critical value of $\Gamma_2(E)$ should not retain sufficient coherence to contribute to the superfluidity in the ground state[45], thus leading to the ultimate breakdown of cuprate superconductivity as Γ_2^* diverges at low doping.

To test these new hypotheses will require (1) determination of whether the superconducting quasiparticles are actually governed by a pairing gap on the scale of Δ_1 as $p \to 0$ and (2) microscopic identification of the Γ_2 scattering process and its relationship to the energy Δ_0 where segregation of homogeneous from heterogeneous electronic structure begins.

Received 22 June 2007; accepted 22 February 2008; published 23 March 2008.

References

1. Kohsaka, Y. *et al.* An intrinsic bond-centered electronic glass with unidirectional domains in underdoped cuprates. *Science* **315**, 1380–1385 (2007).
2. Balatsky, A. V., Vekhter, I. & Zhu, J. X. Impurity-induced states in conventional and unconventional superconductors. *Rev. Mod. Phys.* **78**, 373–433 (2006).
3. Hussey, N. E. Low-energy quasiparticles in high-T_c cuprates. *Adv. Phys.* **51**, 1685–1771 (2002).
4. Fischer, O., Kugler, M., Maggio-Aprile, I., Berthod, C. & Renner, C. Scanning tunneling spectroscopy of high-temperature superconductors. *Rev. Mod. Phys.* **79**, 353–419 (2007).
5. Ørenstein, J. & Millis, A. J. Advances in the physics of high-temperature superconductivity. *Science* **288**, 468–474 (2000).
6. Timusk, T. & Statt, B. The pseudogap in high-temperature superconductors: An experimental survey. *Rep. Prog. Phys.* **62**, 61–122 (1999).
7. Huefner, S., Hossain, M. A., Damascelli, A. & Sawatzky, G. A. Two gaps make a high temperature superconductor. Preprint at <http://arxiv.org/abs/cond-mat/0706.4282> (2007).
8. Campuzano, J. C., Norman, M. R. & Randeria, M. *The Physics of Superconductors* Vol. II, 167–273 (Springer, New York, 2004).
9. Damascelli, A., Hussain, Z. & Shen, Z. X. Angle-resolved photoemission studies of the cuprate superconductors. *Rev. Mod. Phys.* **75**, 473–541 (2003).
10. Anderson, P. W. The resonating valance bond state in La_2CuO_4 and superconductivity. *Science* **235**, 1196–1198 (1987).
11. Zhang, F. C., Gros, C., Rice, T. M. & Shiba, H. A renormalized hamiltonian approach to a resonant valence bond wavefunction. *Supercond. Sci. Technol.* **1**, 36–46 (1988).
12. Kotliar, G. A resonating valence bonds and d-wave superconductivity. *Phys. Rev. B* **37**, 3664–3666 (1988).
13. Paramekanti, A., Randeria, M. & Trivedi, N. Projected wave functions and high temperature superconductivity. *Phys. Rev. Lett.* **87**, 217002 (2001).
14. Anderson, P. W. *et al.* The physics behind high-temperature superconducting cuprates: The 'plain vanilla' version of RVB. *J. Phys. Condens. Matter* **16**, R755–R769 (2004).
15. Chakravarty, S., Laughlin, R. B., Morr, D. K. & Nayak, C. Hidden order in the cuprates. *Phys. Rev. B* **63**, 094503 (2001).
16. Varma, C. M. Non-Fermi-liquid states and pairing instability of a general model of copper oxide metals. *Phys. Rev. B* **55**, 14554–14580 (1997).
17. Honerkamp, C., Fu, H. C. & Lee, D. H. Phonons and d-wave pairing in the two-dimensional Hubbard model. *Phys. Rev. B* **75**, 014503 (2007).
18. Newns, D. M. & Tsuei, C. C. Fluctuating Cu–O–Cu bond model of high-temperature superconductivity. *Nature Phys.* **3**, 184–191 (2007).
19. Valla, T. *et al.* Evidence for quantum critical behavior in the optimally doped cuprate $Bi_2Sr_2CaCu_2O_{8+\delta}$. *Science* **285**, 2110–2113 (1999).

20. Yamasaki, T. *et al.* Unmasking the nodal quasiparticle dynamics in cuprate superconductors using low-energy photoemission. *Phys. Rev. B* **75**, 140513 (2007).
21. Valla, T. *et al.* Fine details of the nodal electronic excitations in $Bi_2Sr_2CaCu_2O_{8+\delta}$. *Phys. Rev. B* **73**, 184518 (2006).
22. Basov, D. N. & Timusk, T. Electrodynamics of high-T_c superconductors. *Rev. Mod. Phys.* **77**, 721–779 (2005).
23. Valla, T. *et al.* Temperature dependent scattering rates at the Fermi surface of optimally doped $Bi_2Sr_2CaCu_2O_{8+\delta}$. *Phys. Rev. Lett.* **85**, 828–831 (2000).
24. Kaminski, A., Fretwell, H. M., Norman, M. R., Randeria, M. & Rosenkranz, S. Momentum anisotropy of the scattering rate in cuprate superconductors. *Phys. Rev. B* **71**, 014517 (2005).
25. Gedik, N., Yang, D. S., Logvenov, G., Bozovic, I. & Zewail, A. H. Nonequilibrium phase transitions in cuprates observed by ultrafast electron crystallography. *Science* **316**, 425–429 (2007).
26. Tinkham, M. *Introduction to Superconductivity* (McGraw-Hill, New York, 1996).
27. Dynes, R. C., Narayanamurti, V. & Garno, J. P. Direct measurement of quasiparticle-lifetime broadening in a strong-coupled superconductor. *Phys. Rev. Lett.* **41**, 1509–1512 (1978).
28. Norman, M. R., Randeria, M., Ding, H. & Campuzano, J. C. Phenomenological models for the gap anisotropy of $Bi_2Sr_2CaCu_2O_8$ as measured by angle-resolved photoemission spectroscopy. *Phys. Rev. B* **52**, 615–622 (1995).
29. Lang, K. M. *et al.* Imaging the granular structure of high-T_c superconductivity in underdoped $Bi_2Sr_2CaCu_2O_{8+\delta}$. *Nature* **415**, 412–416 (2002).
30. McElroy, K. *et al.* Coincidence of checkerboard charge order and antinodal state decoherence in strongly underdoped superconducting $Bi_2Sr_2CaCu_2O_{8+\delta}$. *Phys. Rev. Lett.* **94**, 197005 (2005).
31. McElroy, K. *et al.* Atomic-scale sources and mechanism of nanoscale electronic disorder in $Bi_2Sr_2CaCu_2O_{8+\delta}$. *Science* **309**, 1048–1052 (2005).
32. Gomes, K. K. *et al.* Visualizing pair formation on the atomic scale in the high-T_c superconductor $Bi_2Sr_2CaCu_2O_{8+\delta}$. *Nature* **447**, 569–572 (2007).
33. Howald, C., Fournier, P. & Kapitulnik, A. Inherent inhomogeneities in tunneling spectra of $Bi_2Sr_2CaCu_2O_{8-x}$ crystals in the superconducting state. *Phys. Rev. B* **64**, 100504 (2001).
34. McElroy, K. *et al.* Relating atomic-scale electronic phenomena to wave-like quasiparticle states in superconducting $Bi_2Sr_2CaCu_2O_{8+\delta}$. *Nature* **422**, 592–596 (2003).
35. Hanaguri, T. *et al.* Quasiparticle interference and superconducting gap in $Ca_{2-x}Na_xCuO_2Cl_2$. *Nature Phys.* **3**, 865–871 (2007).
36. Nunner, T. S., Andersen, B. M., Melikyan, A. & Hirschfeld, P. J. Dopant-modulated pair interaction in cuprate superconductors. *Phys. Rev. Lett.* **95**, 177003 (2005).
37. Quinlan, S. M., Hirschfeld, P. J. & Scalapino, D. J. Infrared conductivity of a $d_{x^2-y^2}$-wave superconductor with impurity and spin-fluctuation scattering. *Phys. Rev. B* **53**, 8575 (1996).
38. Dahm, T. Anisotropy of the quasiparticle damping in the high-T_c superconductors $Bi_2Sr_2CaCu_2O_8$ and $YBa_2Cu_3O_{6.9}$ as seen from angle-resolved photoemission experiments. *Phys. Rev. B* **54**, 10150–10154 (1996).
39. Franz, M. & Millis, A. J. Phase fluctuations and spectral properties of underdoped cuprates. *Phys. Rev. B* **58**, 14572–14580 (1998).
40. Millis, A. J. & Norman, M. Antiphase stripe order as the origin of electron pockets observed in 1/8-hole-doped cuprates. *Phys. Rev. B* **76**, 220503(R) (2007).
41. Kanigel, A. *et al.* Evolution of the pseudogap from Fermi arcs to the nodal liquid. *Nature Phys.* **2**, 447–451 (2006).
42. Tanaka, K. *et al.* Distinct Fermi-momentum-dependent energy gaps in deeply underdoped Bi2212. *Science* **314**, 1910–1913 (2006).
43. Boyer, M. C. *et al.* Imaging the two gaps of the high-temperature superconductor $Bi_2Sr_2CuO_{6+x}$. *Nature Phys.* **3**, 802–806 (2007).
44. Graser, S., Hirschfeld, P. J. & Scalapino, D. J. Local quasiparticle lifetimes in a *d*-wave superconductor. Preprint at <http://arxiv.org/abs/cond-mat/0801.0101> (2007).
45. Chubukov, A. V., Norman, M. R., Millis, A. J. & Abrahams, E. Gapless pairing and the Fermi arc in the cuprates. *Phys. Rev. B* **76**, 180501 (2007).

Acknowledgements

We acknowledge and thank D. Dessau, E. W. Hudson, P. Johnson, D. H. Lee, P. A. Lee, A. P. Mackenzie, A. Millis, M. Norman, N. P. Ong, M. Randeria, D. J. Scalapino, K. Shen, T. Timusk, Y. Uemura and T. Valla for helpful conversations and communications. This work is supported by NSF through the Cornell Center for Material Research, by the Cornell Theory Center, by Brookhaven National Laboratory under Contract No. DE-AC02-98CH1886 with the US Department of Energy, by US Department of Energy Awards DE-FG02-06ER46306 and DE-FG02-05ER46236, by the US Office of Naval Research and by Grant-in-Aid for Scientific Research from the Ministry of Science and Education (Japan) and the 21st-Century COE Program for JSPS. Fellowship support is acknowledged by K.F. from I^2CAM.

Correspondence and requests for materials should be addressed to J.C.D.

Supplementary Information accompanies this paper on www.nature.com/naturephysics.